Deciphering circulating tumor cells binding in a microfluidic system thanks to a parameterized mathematical model

Giorgia Ciavolella[1] Julien Granet[1] Jacky G. Goetz [2] Naël Osmani[2]
Christèle Etchegaray[1] Annabelle Collin[1]

October 11, 2023

Abstract

Metastatic spread is a crucial process in which some questions remain unanswered. In this work, we focus on tumor cells circulating in the bloodstream, so-called Circulating Tumor Cells (CTCs). We aim to characterize their trajectories under the influence of hemodynamic forces and adhesion forces resulting from interaction with an endothelial layer using *in vitro* measurements performed with a microfluidic device. This essential step in tumor spread precedes intravascular arrest and metastatic extravasation. Our strategy is based on a differential equation model – a Poiseuille model for the fluid velocity and an ODE system for the cell adhesion model – and allows us to separate the two phenomena underlying cell motion: transport of the cell through the fluid and adhesion to the endothelial layer. A robust calibration procedure enables us to characterize the dynamics. Our strategy reveals the expected role of the glycoprotein CD44 compared to the integrin ITGB1 in the deceleration of CTCs and quantifies the strong impact of the fluid velocity in the protein binding.

2010 *Mathematics Subject Classification.* 62-07; 65L09; 76Z99; 97M60;
Keywords and phrases. Differential equations; Parameter estimation; Circulating tumor cells; Biological data

1 Introduction

One of the most important and deadly features of solid tumors is the increased ability of cancer cells to migrate and invade other organs, which is called metastatic spread. In the last 70 years the number of cancer deaths registered with metastasis has tripled [1]. Different tumors have substantial incidence variation. However, metastasis is the major source of cancer-related death [2].

[1]Inria, Univ. Bordeaux, CNRS, Bordeaux INP, IMB, UMR 5251, F-33400 Talence, France
[2]INSERM UMR_S 1109, Univ. Strasbourg, FMTS, Équipe labellisée Ligue Contre le Cancer, F-67000 Strasbourg, France.

The blood and lymphatic circulations are used as a means of transport to reach distant organs. Tumor cells that have previously detached from a primary tumor can invade the surrounding extracellular matrix. Successful intravasation into the vessels means that cancer cells can now leave the original site. Inside the blood vessels, hostile conditions prevail. Circulating Tumor Cells (CTCs) are subjected to physical stresses that include hydrodynamic flow and loss of attachment to a substrate, as well as other obstacles involving the human immune system (and platelets) [3, 4]. These factors lead to a significant decrease in the number of CTCs and also to their eventual clustering. The remaining single cells or small cell clusters eventually extravasate, reaching a secondary site where they either stay dormant or form a new tumor [5].

CTCs receive much research interest due to their therapeutic potential in liquid biopsy [6, 7]. Indeed, they could allow to monitor tumor heterogeneity or response to a treatment, but also to detect the minimal residual disease, and serve as a prognosis biomarker or as a target for personalized therapies [8–10]. However, the detection, identification and characterization of CTCs present important challenges due to their heterogeneity and low abundance [11]. From the biological standpoint, understanding the key steps involved in CTCs arrest on the endothelial wall is crucial to explain secondary tumour locations. Indeed, the possibility of extravasating is permitted by CTCs arrest and firm adhesion to the vascular endothelium, phenomena that need further insights [12–16].

Studies previously pursued by biologists Follain et al. [13] and Osmani et al. [14] have deepened into the mechanical cues that promote CTCs successful arrest and extravasation. In [13], they have shown that an optimal flow is required for CTCs to arrest on the endothelium of the vascular wall. Furthermore, in [14], they have identified the adhesion receptors at play. Early adhesion is mediated by the glycoprotein CD44, involved in a weak form of bonds, while integrin ITGB1 favors stabilization of the adhesions. The team of biologists have performed both *in vitro* and *in vivo* experiments. *In vitro* experiments consist in using a microfluidic channel with controlled fluid velocity (simulating a blood vessel) into which tumor cells are injected. *In vivo* experiments are led on zebrafish embryos where they can follow CTCs pumped by the heart along the vascular architecture. In the present work, these *in vitro* data will be exploited in combination with mathematical modeling.

Various theoretical models of cell adhesion have been developed over time. First studies have focused on the binding dynamics of a single bond in a kinetic setting [17, 18], while bonds clusters sharing a constant or varying load have been considered in [19–21]. In the case of inflow cell dynamics, several biological questions can be addressed, such as the emergence of several cell displacement regimes (freely-flowing, rolling, slipping, stationary arrest) with possible bistability or shear-threshold effect between them. A related issue concerns the bonds response to hydrodynamic forces, with *catch bonds* whose lifetime increases with load, *slip bonds* for which it decreases exponentially with load (so-called Bell's law), or a combination of both depending on the shear rate.

First computational approaches allowed to describe a hard sphere submitted to hydrodynamics forces and stochastic binding interaction with the wall [22–24]. This framework has been applied to leukocytes adhering through L-selectin ligands [25–27]. A simpler setting with slip bonds allowed to obtain analytical characterizations [28]. In [29, 30], the adhesion of a rolling sphere is described following the membrane approaching the wall at the front, and detaching at the rear, for catch-slip bonds. Numerical simulations illustrate the effect of shear rate on the steady state. In [31], both translational and rotational motions of a spherical cell are affected by elastic bonds. This allows to explain the interplay between rolling and slipping, and provides a numerical state diagram of leukocyte motion. Theoretical models can also take ligands positions into account, thus enabling bonds tilting and subsequent cell sliding. The transition between rolling and sliding for a critical shear rate is established for a rigid cylinder in [32], where elastic

bonds are described by a distribution function structured by position. This continuum framework is also used in mathematical modeling approaches in deterministic [33–35] and stochastic [36] settings. In the same spirit but in the absence of space structure, stochastic and deterministic models are developed for a particle cell in [37]. Mathematical analysis provides a parameter space for cell regimes together with an explicit formula for the mean arrest time. Although minimal in the hydrodynamics description, these models have less parameters and are therefore more suited to calibration with experimental data.

Theoretical frameworks have been confronted to microfluidics experiments on CTCs in [38–40]. First, using an empirical model, the authors investigate cell detachment in response to fluid acceleration for N-cadherin based adhesion [38]. Motivated by CTCs isolation in liquid biopsies, they also consider cells arrest on a wall coated with EpCAM (epithelial-cell adhesion molecules) antibodies [39]. Finally, in [40], the authors perform microfluidics experiments to study the effect of the shear rate on the dynamics of breast cancer cells interacting with an EpCAM-coated wall. Three regimes were observed (freely-flowing, firmly adhering, and rolling/slipping). Experimental data consisted in trajectories and in stopping times and lengths that were used to empirically calibrate a model based on [31]. More precisely, the cell-wall gap, the typical adhesion force and the spring constant were sequentially identified by numerical investigations. Then, the cell velocity during capture was well fitted by a decreasing exponential function, yielding a typical decreasing time characteristic of the cell-wall interaction.

In this work, we aim to capture the role of adhesion proteins and hydrodynamic forces and to understand their interplay focusing on the first phase of CTCs interaction with the endothelial wall. We use a Poiseuille model for the fluid velocity, and weakly couple it to a modification of the model proposed in [36, 37]. This modeling approach allows its rigorous calibration using the *in vitro* experiments carried out by Osmani and collaborators, see [14, 41]. In this model, the cell velocity depends on both the fluid velocity and the bonds density, while the binding dynamics takes into account bonds formation, adhesion growth, and unbinding.

The work is arranged as follows. Section 2 contains the main information about the biological data. More specifically, the data consist of 9 videos of CTCs transported by the fluid at 3 different velocities and with 3 different cell types (control, ITGB1-depleted, and CD44-depleted cells), see Subsection 2.1 for protocol details and Subsection 2.2 for data presentation. Trajectories and velocities of 149 cells were extracted from these data. Section 3 is devoted to methods. After a brief statistical analysis of the data in Subsection 3.1, which shows the statistically significant slowing behavior of CTC velocities over time in most cases, Subsections 3.2 and 3.3 present the mathematical modeling. In Subsection 3.4, a strategy for parameter estimation of this model is presented. The results showing the good agreement of the model with the data are presented in Section 4. A discussion is presented in Section 5, and finally, conclusions are given in Section 6. An important result is that the estimated values of the parameters allow the deciphering of the CTC binding. Indeed, this work demonstrates the expected role of the glycoprotein CD44 compared with the integrin ITGB1 in slowing CTCs. It also allows quantification of the strong influence of fluid velocity on protein binding.

2 Data

In this Section, we present the experimental data, beginning with their acquisition and ending with their extraction. First, in Subsection 2.1 we present the experimental protocol. Then, in Subsection 2.2, we show what kind of data are obtained, and briefly present the tracking techniques used to extract the trajectory and velocity of 149 cells. We then present the resulting cell velocities.

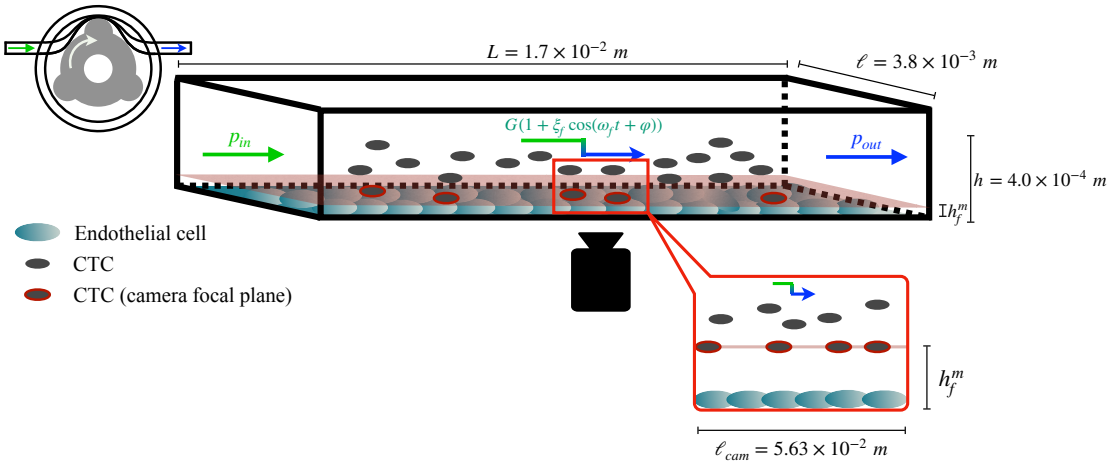

Figure 1: Experimental setup. A rectangular microfluidic channel (black box) contains an endothelial layer (turquoise cells) and a fluid containing **DA21** tumor cells (grey cells). The fluid is pumped by a peristaltic pump (left in the figure) with a pressure gradient $G(1+\xi_f \cos(\omega_f t+\varphi))$ at the entrance. A camera is placed to record the motion of cells located in a focal plane at a distance h_f^m from the endothelial layer (grey cells surrounded by a red contour), see [41].

2.1 Protocol

We consider in this work *in vitro* experiments. Human Umbilical Vein Endothelial cells (**HUVEC**, Promocell) were seeded at 30 000 cells per channel in a rectangular microfluidic channel (IBIDI) of length $L = 1.7 \times 10^{-2}$ m, of width $l = 3.8 \times 10^{-3}$ m and height $h = 4.0 \times 10^{-4}$ m. Medium was changed twice a day until they reach maximal confluency (3 to 4 days). **DA21** mouse breast carcinoma cells were with siRNA using Lipofectamine RNAiMAX (Thermo Fisher) following the manufacturer's instructions. Experiments were performed between 72 hours and 96 hours post-transfection. 3 days after siRNA transfection, **DA21** cells were resuspended at a concentration of 10^6 cells/ml in a Hépès-buffered cell culture medium and perfused into the channel using using a REGLO Digital MS-2/12 peristaltic pump (Ismatec), Tygon LMT-55 3-stop tubing (IDEX), 0.5 and 1.6 mm silicon tubing and elbow Luer connectors (IBIDI).

In the setup of the pump, the mean value of the entry pressure gradient is fixed and denoted by G. The fluid velocity generated – which contains oscillations due to the pump – depends on the position in the channel and is not measured. A cMOS camera (IDS) is placed to record the motion of cells located in a focal plane at a distance h_f^m from the endothelial layer. The experimental data consist of timelapse movie acquired at a rate of 24 frame per seconds for 2 minutes, on a rectangle of width $\ell_{cam} = 5.63 \times 10^{-4}$ m and of height $h_{cam} = 2.99 \times 10^{-4}$ m The setup is shown in Figure 1.

2.2 Data availability

An example of a video image is shown in Figure 2. The cells forming the endothelial layer are seen in the background, whereas moving CTCs that are not in the focal plane of the camera are seen in the foreground. These CTCs have a well-defined shape, so that their trajectories can easily be followed while they appear in the video. Most cells are smoothly transported through

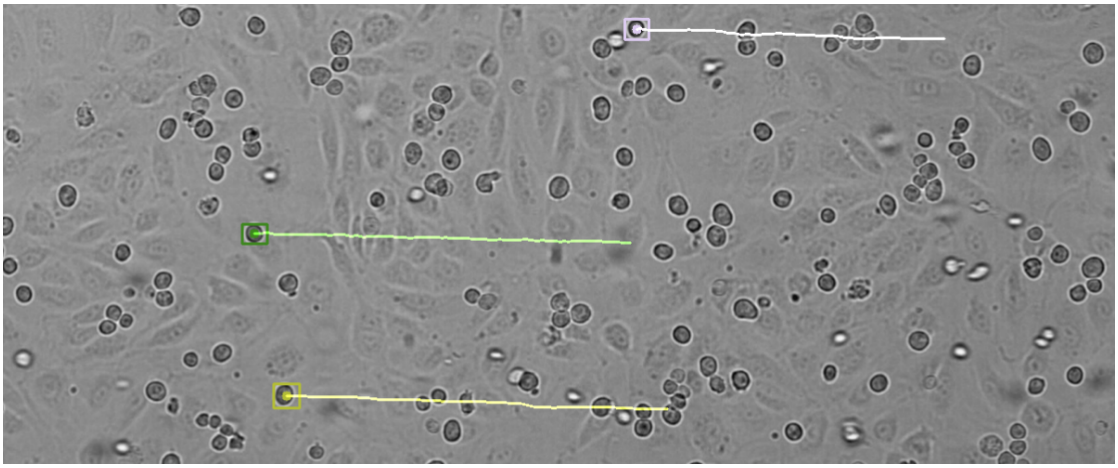

Figure 2: Example of the use of the CSRT tracker on three different cells of the video corresponding to the control case (siCTL) at a fluid velocity corresponding to the smallest pressure gradient $G^{(1)} = 50.33$ Pa.m^{-1}.

the fluid. Sometimes, a cell stops on the endothelial layer. This arrest can be stable, meaning that the cell remains attached to the endothelial layer, or unstable, *i.e.* the cell can detach due to a collision with other cells or under the effect of the hydrodynamics forces. However, in this work we focus only on non-arrested cells.

The different experimental subgroups are summarized in Table 1. Experiments have been realized keeping the fluid at a controlled pressure gradient by the peristaltic pump. Three values of pressure gradient have been considered: $G^{(1)} = 50.33$ Pa.m^{-1}, $G^{(2)} = 100.66$ Pa.m^{-1} and $G^{(3)} = 201.32$ Pa.m^{-1}. For each of these cohorts, small interfering RNA (siRNA) depletion of adhesion proteins gives rise to three sub-cohorts, see Western-blot results in Supplementary materials in [14]:

- siCTL: control group (D2A1 cells treated with a CTL siRNA);
- siITGB1: depletion of integrin ITGB1 (D2A1 cells treated with a siRNA targeting ITGB1);
- siCD44: depletion of CD44 (D2A1 cells treated with a siRNA targeting CD44).

G \ Protein modification	**siCTL**	**siITGB1**	**siCD44**	Total
50.33 Pa.m^{-1}	15 (15)	15 (16)	12 (14)	**42** (45)
100.66 Pa.m^{-1}	14	20	9 (11)	**43** (45)
201.32 Pa.m^{-1}	24 (29)	14	14 (16)	**52** (59)
Total	**53** (58)	**49** (50)	**35** (41)	**137** (149)

Table 1: Total number of cells considered in each cohort and sub-cohort after removing the outliers. The values in parenthesis correspond to the number of tracked cells.

We collect cell trajectories from the 9 different videos (3 different pressure gradients $\times$ 3 different proteins expressions). For the two first values of pressure gradient, we use a semi-automatic tracker called *Channel and Spatial Reliability Tracker* (CSRT) that consists in first

manually designing a box surrounding the cell of interest and second automatically recording the box evolution at each frame of the video [42], see Figure 2. In the videos realised with the highest pressure gradient, the mean fluid velocity is too high for the tracker to automatically track the CTCs. For this reason, they were tracked manually. By deriving the trajectories using a first-order scheme, we can directly determine the cell velocities. Note that the tracking procedure captures only the translational motion. Therefore, the data used in this work do not allow discussing possible CTCs rolling.

Table 1 summarizes the number of cells considered in each of the nine videos. For each velocity cohort, at least 40 cells were considered. Some cells were significantly different from the others since they had very high initial velocities. We assumed that they either collided with another cell before entering the video time-lapse, or that they were located in a different focal plane, and we excluded them. These outliers make up only a small portion of the data, since they counted for at most 5 for each velocity cohort (12 for 149 cells $\sim 8\%$), see Table 1 for details.

The extracted velocities over time of the $N_{cell} = 137$ cells are given in Figure 3. Individual cell velocities are in transparent color and weighted mean across cells is shown in normal color. The choice of weighted means is motivated by a better visualisation of the results, since the noise is reduced. The strategy to obtain these weighted means is detailed in Subsection 3.1. The red curves correspond to siCTL cells, green to siITGB1 cells, and blue to siCD44 cells. For each figure, the straight lines correspond to the linear regressions of the weighted means of velocities after adjustment of the initial time in order to synchronize the oscillations. The data are normalized by 100, 200 and 400 µm.s^{-1}. We normalize the data in order to facilitate the comparison between the different cohorts. The values considered will be explained later in Section 4.2. However, it should be noted that the ratio between the selected velocities is equal to the ratio of the pressure gradients.

3 Methods

This study aims at deciphering the influence of hydrodynamic and adhesion forces on the dynamics of CTCs moving in interaction with the wall of a microfluidic device. First, we perform a brief statistical examination of the tracked cell velocities in Subsection 3.1. Second, a fluid velocity model is presented in Subsection 3.2. Third, a model for CTCs velocity under both hydrodynamic transport and adhesion to the wall is derived in Subsection 3.3. Finally, in Subsection 3.4 we fit the model to the experimental data using a well-designed technique for parameter estimation.

All statistical analyses were performed with `R`. For the t-tests, we use the `t_test` function of the library `rstatix`.

3.1 Quick statistical analysis of the data

We perform a preliminary statistical analysis of the velocity data shown in Figure 3. The raw data are preprocessed as follows. First, the velocities are normalized with respect to the fluid pressure cohort, to remove the linear dependence on the fluid velocity. Each velocity in transparent color is corrected for phase shift to synchronize the oscillations. To do so, we use the estimated cell velocities aligning their maximum points over two periods of oscillation. Finally, spurious data are filtered, to deal with the additional noise brought by the first-order derivation of velocities from positions. Indeed, some velocity values can be artificially large or low and perturb the analysis. To deal with this difficulty, we compute weighted means assigning a null weight on values above 0.85 µm.s^{-1} and below 0.35 µm.s^{-1}.

We perform a quick statistical analysis of these velocities between the different cohorts and subcohorts. First, we run t-tests of the mean velocity values to determine if the differences

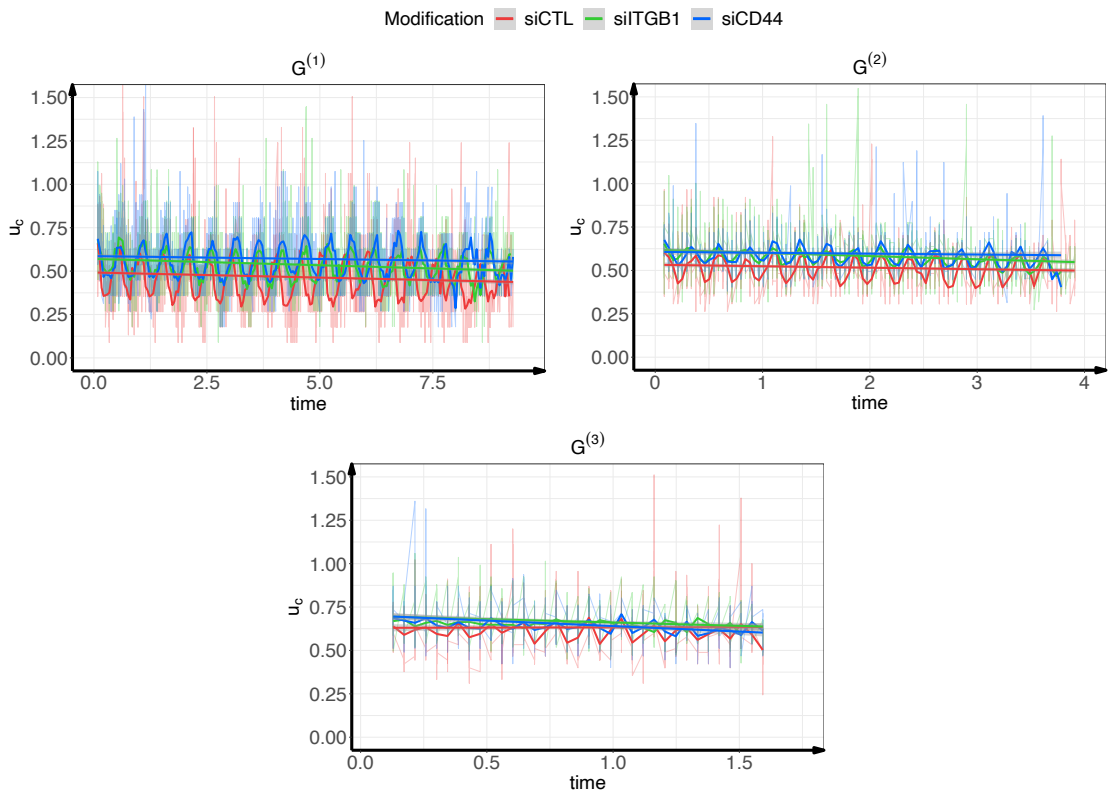

Figure 3: All extracted cell velocities over time (137 cells, without outliers). Cell velocities are given in transparent color and weighted mean across cells is shown in normal color. The choice of weighted means is motivated by a better visualisation of the results, since the noise is reduced. The three figures correspond to the three different pressure gradient cohorts: top left for $G^{(1)}$, top right for $G^{(2)}$ and bottom for $G^{(3)}$. The red curves stand for the siCTL cases, green for siITGB1 cases, and blue for siCD44 cases. For each figure, the straight lines correspond to the linear regressions of the weighted means of cell velocities. The initial time of each cell velocity is adjusted in order to synchronize the oscillations. The data are normalized respectively by 100, 200 and 400 µm.s^{-1}.

between cohorts and subcohorts are significant. Second, we run linear regressions on the velocity values and use them to determine for which cohort and subcohort the observed decreases are significant.

3.2 Fluid velocity modeling

In this subsection, we derive a model for the fluid dynamics in the microfluidic device. When the viscous effects of the fluid prevail over convection, the Navier-Stokes equations can be reduced to a Poiseuille equation. In that case, the flow shows a parabolic profile at each time, with a maximal velocity in the center of the channel decreasing to zero at the walls. In case of a time-independent pressure gradient, the Poiseuille regime is valid when the fluid verifies the following properties :

(1) it is incompressible and Newtonian ;

(2) the gravitational effect on the fluid is negligible;

(3) its flow is laminar ;

(4) and its velocity profile does not evolve over the pipe's length denoted by L in what follows.

Conditions 1 and 2 are allowed when working with a microfluidic device where the fluid is mainly comparable to water. Condition 3, can be checked by calculating the Reynolds number given by

$$Re = \frac{\rho\, Q\, D_h}{\mu\, S},$$

where ρ is the fluid density, Q the volumetric flow rate, μ the dynamic viscosity, $D_h = \frac{2(l\times h)}{l+h}$ the hydraulic diameter of a fully submerged rectangular channel and $S = l \times h$ the cross-section surface. The density can be taken as $\rho = 1.00 \times 10^3$ kg.m^{-3}. Based on the experiments and procedure of Osmani and coworkers in [14, 41], we have $D_h = 7.24 \times 10^{-4}$ m, $S = 1.52 \times 10^{-6}$ m^2 and $Q \leq 5.67 \times 10^{-9}$ m^3.s^{-1}. For the dynamic viscosity, one may refer to [43] (Table 2) to obtain a close approximation of the value (different medium, but similar composition when no FBS is added). The corresponding value is $\mu = 7.31 \times 10^{-4}$ Pa.s.

It follows that $Re \leq 3.75$. This value is much smaller than the critical Reynolds number for the transition from a laminar to a turbulent state, that is equal to 2600 in the case of a rectangular tube with a width eight times larger than the height, see [44]. Finally, in order to verify Condition 4, we must determine the hydrodynamic entrance length of our microfluidic device (for more details, see [45], Chapter 8, Section 8.1). For rectangular channels at laminar flow, a formula has been derived in [46]. The hydrodynamic entrance ℓ (in meters) is then given as a non-linear function of the aspect ratio $AR = \frac{h}{l}$ and the Reynolds number Re. Using the upper bound of Re determined previously, a quick computation gives $\ell \leq 1.53 \times 10^{-3}$ m. We can thus consider the Poiseuille flow to be fully developed (*e.g.* independent of the length L) if we observe at least 1.53×10^{-3} m away from the pipe inlet. According to the protocol given in [41] the data was collected as close as possible to the center of the device lengthwise, which is at about 8.50×10^{-3} m meters away from the inlet.

In our case, however, the hypothesis of a time-independent pressure gradient is not valid. In fact, the fluid dynamics is affected by the angular velocity of the pump rotor, leading to a time-dependent oscillatory perturbation term to the pressure gradient term, which we model as follows

$$G(1 + \xi_f \cos(\omega_f t + \varphi)),$$

where ξ_f is the multiplicative correction amplitude, ω_f the angular velocity, and φ the cell-dependent phase shift.

When working with an oscillating pressure gradient, the condition for the establishment of a parabolic velocity profile is strongly tied to the frequency of the oscillation relative to the viscosity of the fluid. Such relation is given through a dimensionless coefficient $\mathbf{Wo} = \frac{h}{2}\sqrt{\frac{\omega_f \rho}{\mu}}$ introduced by Womersley in [47], which has to be inferior to 1 when the mean value of the pressure gradient is zero. A non-zero mean value will however relax such constraint, and using the results from [48] along with supplementary observations, one can readily show a parabolic profile is obtained in our case, see Remark 3.1 and Supplementary Material A.3 for more details. The fluid velocity can therefore be written as

$$\frac{G}{2\nu\rho} h_f^m (h - h_f^m) + \xi_f \frac{G}{\rho\omega_f} i \left(\frac{\sinh(Zh_f^m) + \sinh(Z(h - h_f^m))}{\sinh(Zh)} - 1 \right) e^{i(\omega_f t + \varphi)}, \tag{1}$$

where i is the imaginary unit and $Z = (1+i)\sqrt{\frac{\omega_f}{2\nu}}$ with $\nu = \frac{\mu}{\rho}$ the kinematic viscosity. We recall that h_f^m is the distance between the wall and cells in the focal plane and $h = 4.00 \times 10^{-4}$ m is the channel height. Taking the real part of this solution and performing computations (based on the linearity of the system and the principle of superposition), the fluid velocity in our context writes

$$u_f(t) = \bar{u}_f(h_f^m) + i_f(h_f^m, \xi_f, \omega_f)\cos(\omega_f t + \varphi) + r_f(h_f^m, \xi_f, \omega_f)\sin(\omega_f t + \varphi), \tag{2}$$

where

$$\begin{aligned} \bar{u}_f(h_f^m) &= \frac{G}{2\nu\rho} h_f^m (h - h_f^m), \\ r_f(h_f^m, \xi_f, \omega_f) &= \frac{\xi_f G}{\omega_f \rho} \mathrm{Re}\left(1 - \frac{\sinh(Zh_f^m) + \sinh(Z(h - h_f^m))}{\sinh(Zh)} \right), \\ i_f(h_f^m, \xi_f, \omega_f) &= \frac{\xi_f G}{\omega_f \rho} \mathrm{Im}\left(1 - \frac{\sinh(Zh_f^m) + \sinh(Z(h - h_f^m))}{\sinh(Zh)} \right). \end{aligned}$$

Note that $\bar{u}_f$ is the mean fluid velocity, while the unknown parameters are h_f^m, ξ_f, ω_f and φ.

Remark 3.1. *Numerical approximations for the full device were also performed to test the hypothesis and investigate its limitations. These results confirming our fluid modelling can be found in the Supplementary Materials A. More specifically, we begin by verifying the value of the hydrodynamic entrance length, see Subsection A.1, and we follow with validation of the fluid expression in Subsection A.2. A final subsection A.3 focuses on how the non-zero mean value of the pressure gradient allows us to work with a Poiseuille velocity profile.*

3.3 Cells velocity modeling

In this subsection, we define a deterministic model for cell motion based on a coupling between fluid velocity and adhesion dynamics, following previous studies [36, 37]. The interest is in capturing the different behaviours induced by varying fluid velocity and the number of expressed proteins. Both changes have an impact on cells velocity.

By denoting N the bonds density and u_c the cell velocity, the model writes $\forall t > 0$,

$$\begin{cases} N'(t) = c + (r - d)N, \\ u_c(t) = u_f(t) - B(u_f(t), u_c(t))\, N(t), \end{cases} \tag{3}$$

together with the initial condition $N(0) = 0$. In System (3), c, r, d are given in s^{-1} and stand respectively for the global binding rate, the growth rate and the unbinding rate. The function B accounts for the velocity decrease arising from a unit adhesion density. All parameters are nonnegative.

Assumption 3.1. *We assume that the adhesion parameters are time-independent and depend only on the mean fluid velocity:*

$$c = c(\bar{u}_f),\ r = r(\bar{u}_f),\ \text{ and } d = d(\bar{u}_f).$$

This amounts to neglecting the effects of fluid velocity oscillations on the binding dynamics.

The function B can depend either on fluid velocity or on the cell one. Three models are considered:

1. Constant force model: $B(u_f(t), u_c(t)) = b$, where b (in $\mu\mathrm{m.s}^{-1}$) quantifies the absolute velocity decrease induced by each unit of bonds density.
2. Fluid-dependent force model: $B(u_f(t), u_c(t)) = b\, u_f(t)$, with b is the dimensionless proportion of velocity decrease induced by each unit of bonds density.
3. Cell-dependent force model: $B(u_f(t), u_c(t)) = b\, u_c(t)$, where b is the dimensionless parameter for the friction ratio between bonds stiffness and fluid viscosity.

Assumption 3.2. *We consider the cell-dependent model for the cell velocity equation:*

$$B(u_f(t), u_c(t)) = b\, u_c(t).$$

Under Assumptions (3.1)-(3.2), System (3) has an explicit solution. If $d - r \neq 0$, we obtain for $t > 0$

$$N(t) = \frac{c}{d-r}(1 - e^{-(d-r)t}), \tag{4}$$

and then

$$u_c(t) = \frac{u_f(t)}{1 - \frac{bc}{d-r}(e^{-(d-r)t} - 1)}. \tag{5}$$

Note that at $u_c(0) = u_f(0)$, so that the cell has not formed adhesion bonds at initial time. On the other hand, experimental observations may occur only after the cell has initiated an adhesive interaction with the wall. This is why we introduce an additional parameter $\tau \geq 0$ that stands for the observation time lag. A cell with a small value of τ would be observed with an initial velocity approaching the fluid velocity, while a cell with a large value of τ would be entering the observation zone with a lower velocity.

Finally, the percentage of decrease between the cell and the fluid velocities at time $t \geq 0$ is given by the quantity $1 - \frac{u_c}{u_f}(t)$. Its limit as $t \to \infty$ then quantifies the asymptotic cell regime, and is given by

$$d_{\%} := \frac{bc}{d - r + bc}.$$

To conclude, our coupled model of parameters h_f^m, ξ_f, ω_f, φ, τ, b, c, r and d reads

$$\begin{aligned} u_f(t) &= \bar{u}_f(h_f^m) + i_f(h_f^m, \xi_f, \omega_f)\cos(\omega_f t + \varphi) + r_f(h_f^m, \xi_f, \omega_f)\sin(\omega_f t + \varphi), \\ u_c(t) &= u_f(t)/(1 - \tfrac{bc}{d-r}(e^{-(d-r)(t+\tau)} - 1)). \end{aligned} \tag{6}$$

3.4 Parameters estimation

We calibrate the model using a well-adapted estimation procedure. The main difficulties in fitting our model to the data are (a) the data noise (see Figure 3), (b) the little information on the fluid velocity, and (c) the fact that the adhesion parameters are strongly correlated with the fluid parameters. Therefore, we choose a mixed-effects parameter estimation procedure. The nonlinear mixed-effects model consists of pooling all subjects in a population and estimating a global distribution of uncertainties in the population to compensate for identifiability problems [49]. For example, the parameters of each cell i could be divided into two types of uncertainties: a first part that is the same for all cells (denoted by θ_{pop} for the parameter θ^i) and corresponds to the fixed effect, and a second part that represents individual variability (denoted by θ^i_{ind}) and corresponds to random effects, *i.e.* $\theta^i = \theta_{pop} + \theta^i_{ind}$. Different covariates can also be added, e.g., for different cohorts of the population. A nonlinear mixed-effect estimation algorithm – called the stochastic approximation expectation maximization (SAEM) algorithm [50] – is implemented in the software `Monolix` [51]. Thanks to the R package `lixoftConnectors`, we could easily run `Monolix` using R. The code and extracted cell velocities are available here (a recent version of `Monolix` is required).

Fluid parameters The only known fluid parameter is the mean pressure gradient given by $G^{(\mathbf{c})} = 2^{\mathbf{c}-1} G^{(1)}$, where $\cdot^{(\mathbf{c})}$ denotes here and in the following the velocity cohort for $\mathbf{c} \in \{1,\ 2,\ 3\}$, and $G^{(1)} = 50.33$ Pa.m^{-1}. Then, for most of fluid parameters, individual variability is not considered. In addition always to avoid identification problems, we strongly incorporate the information we have between the three cohorts by considering

$$h_f^{m\,(\mathbf{c})} = h_f^{m\,(1)} \text{ m}, \quad \omega_f^{(\mathbf{c})} = 2^{\mathbf{c}-1}\,\omega_f^{(1)} \text{ rad.s}^{-1}, \quad \xi_f^{(\mathbf{c})} = 2^{1-\mathbf{c}}\xi_f^{(1)},$$

for $\mathbf{c} \in \{1, 2, 3\}$. The hypothesis on ω_f is obvious and the hypothesis on ξ_f implies that the oscillation amplitude of the pressure gradient is constant as $G^{(\mathbf{c})}\xi_f^{(\mathbf{c})} = G^{(1)}\xi_f^{(1)}$.

Only the phase shift φ depends on the considered cell. This implies that to represent the fluid velocity of the 3 cohorts, 142 parameters must be estimated: 3 fixed effects for $h_f^{m\,(1)}, \omega_f^{(1)}, \xi_f^{(1)}$, 2 fixed effects for φ (mean and standard deviation) and N_{cells} randoms effects for φ.

Adhesion parameters Since b, c, r, and d are strongly paired, they can not be identified independently from the observations. We will then estimate only bc and $d - r$.

The fact that we link all cohorts has the great advantage that we can constrain the values of the fluid parameters, but it introduces a bias in the estimation of the individual variability of the parameters, since the fixed effects are the same for the 3 cohorts. For this reason, we consider cohort covariates for bc:

$$\log(bc^i) = \log(bc_{pop}) + \beta_{bc}^{(2)}[\text{if } \mathbf{c} = 2] + \beta_{bc}^{(3)}[\text{if } \mathbf{c} = 3] + bc^i_{ind}.$$

For the adhesion parameters bc, $d - r$ and τ, the behaviour of the individual cell is integrated meaning that 420 parameters must be estimated: 2×3 fixed effects, 3 covariates for bc and $3N_{cells}$ random effects.

Distribution laws For parameter distributions, we consider *logitnormal* distributions for h_f^m, ξ_f^m, φ and τ to keep them respectively in 0–1.5×10^{-5} m, 0–1, 0–2π, and 0–10 s. We consider *lognormal* distributions for the other parameters. Furthermore, whenever mixed effects are estimated, prior values and prior standard deviations are given to the SAEM algorithm. We will

denote by the superscript $(\cdot)^*$ the priors and by $(\cdot)^s$ the prior standard deviations. We consider

$$(h_f^{m(1)})^* = 7.5 \times 10^{-6} \text{ m}, \ (\omega_f^{(1)})^* = 12 \text{ rad.s}^{-1}, \ (\xi_f^{(1)})^* = 0.3, \ (\varphi)^* = \pi, \ (\varphi)^s = 1,$$
$$(bc)^* = 0.5 \text{ s}^{-1}, \ (bc)^s = 1, \ (d-r)^* = 0.5 \text{ s}^{-1}, \ (d-r)^s = 1, \ (\tau)^* = 0.5 \text{ s}, \ (\tau)^s = 1.$$

Model error We consider a constant error model and we estimate the error model standard deviation starting from the prior value 25. Adding this value to the estimation of the fluid and adhesion parameters, 563 parameters are estimated during the procedure.

4 Results

4.1 Quick statistical analysis of the data

The *p-values* resulting from the t-tests are given in Table 2. The diagonal blocks correspond to comparison between different protein modifications at the same fluid pressure, while the upper diagonal blocks account for comparison of subcohorts having the same protein modification and different fluid pressures. Significant differences can be seen between different protein modifications at the same fluid pressure and between the same protein modifications at different fluid pressure. Indeed, *p-values* are smaller than 2×10^{-3}, except between siITGB1$^{(2)}$ and siCD44$^{(2)}$ ($p = 0.15$) and between siITGB1$^{(3)}$ and siCD44$^{(3)}$ ($p = 0.1$). Thus, at high fluid pressure gradients, the differences depleting the first or second adhesion protein are not relevant, but at smaller pressure gradients they are informative.

	siITGB1$^{(1)}$	**siCD44$^{(1)}$**	**siCTL$^{(2)}$**	**siITGB1$^{(2)}$**	**siCD44$^{(2)}$**	**siCTL$^{(3)}$**	**siITGB1$^{(3)}$**	**siCD44$^{(3)}$**
siCTL$^{(1)}$	$\mathbf{< 10^{-7}}$	$\mathbf{< 10^{-7}}$	$\mathbf{< 10^{-7}}$	-	-	$\mathbf{< 10^{-7}}$	-	-
siITGB1$^{(1)}$	-	$\mathbf{8.0 \times 10^{-4}}$	-	$\mathbf{< 10^{-7}}$	-	-	$\mathbf{< 10^{-7}}$	-
siCD44$^{(1)}$	-	-	-	-	$\mathbf{1.7 \times 10^{-3}}$	-	-	$\mathbf{< 10^{-7}}$
siCTL$^{(2)}$	-	-	-	$\mathbf{< 10^{-7}}$	$\mathbf{< 10^{-7}}$	$\mathbf{< 10^{-7}}$	-	-
siITGB1$^{(2)}$	-	-	-	-	0.15	-	$\mathbf{< 10^{-7}}$	-
siCD44$^{(2)}$	-	-	-	-	-	-	-	$\mathbf{< 10^{-7}}$
siCTL$^{(3)}$	-	-	-	-	-	-	$\mathbf{3 \times 10^{-6}}$	$\mathbf{6.6 \times 10^{-4}}$
siITGB1$^{(3)}$	-	-	-	-	-	-	-	0.10

Table 2: *Resulting p-values from the t-tests performed on the mean velocity values between different protein modifications at the same fluid pressure and between the same protein modification but at different fluid pressures. Superscripts refer to the experiment number with the fluid pressure values as in Subsection 2.2. The bold values are the p-values inferior to* 2×10^{-3}.

The outputs of the linear regressions can be found in Table 3. The intercepts – corresponding to the value of cell velocity at time $t = 0$ – increase with fluid pressure for the same protein modification, and for a given fluid pressure it increases with respect to protein modifications or it remains stable. Anyways, intercepts are always smaller than 1, value corresponding to the normalisation by 100, 200 and 400 µm.s^{-1}. The slope estimate and its *p-value* – related to the adhesions effects during the observation duration – show a significant decrease from the intercept value for almost all cases except for siCD44$^{(2)}$ and siCTL$^{(3)}$.

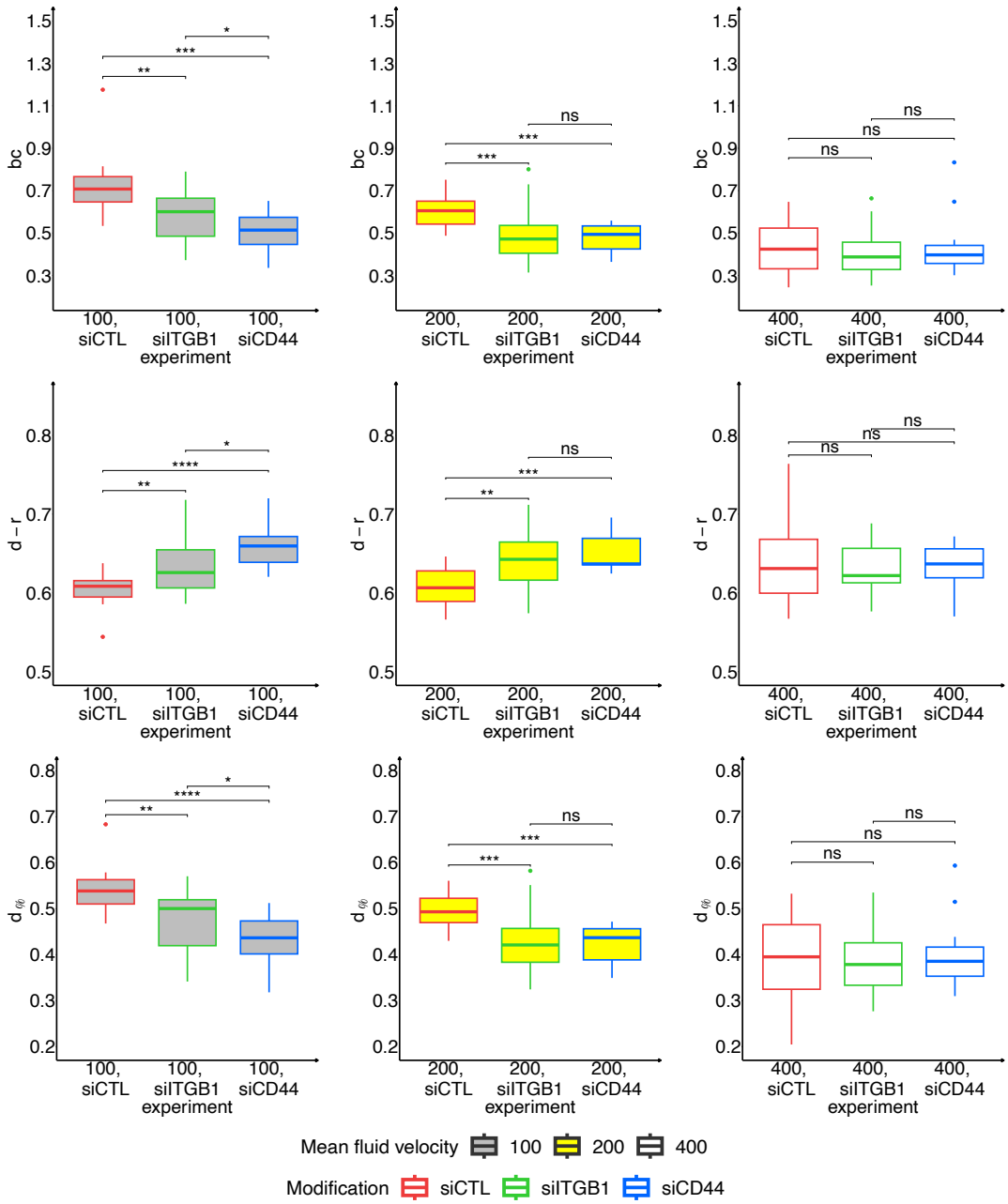

Figure 4: Box plots of the estimated parameters bc (top) and $d-r$ (middle) and the percentage of decrease in cell velocity $d_{\%}$ (bottom) for the 3 cohorts (left: pressure gradient fixed at $G^{(1)}$ corresponding to $\sim$ 100 µm.s^{-1}, middle: $G^{(2)}$ corresponding to $\sim$ 200 µm.s^{-1}, right: $G^{(3)}$ corresponding to $\sim$ 400 µm.s^{-1}) and for all considered cells (red: siCTL, green: siITGB1, blue: siCD44). We substitute p-values with symbols such that: ns correspond to p$>$ 10%, * to p$\leq$ 10%, ** to p$\leq$ 5%, *** to p$\leq$ 0.5%, and **** to p$\leq$ 0.05%.

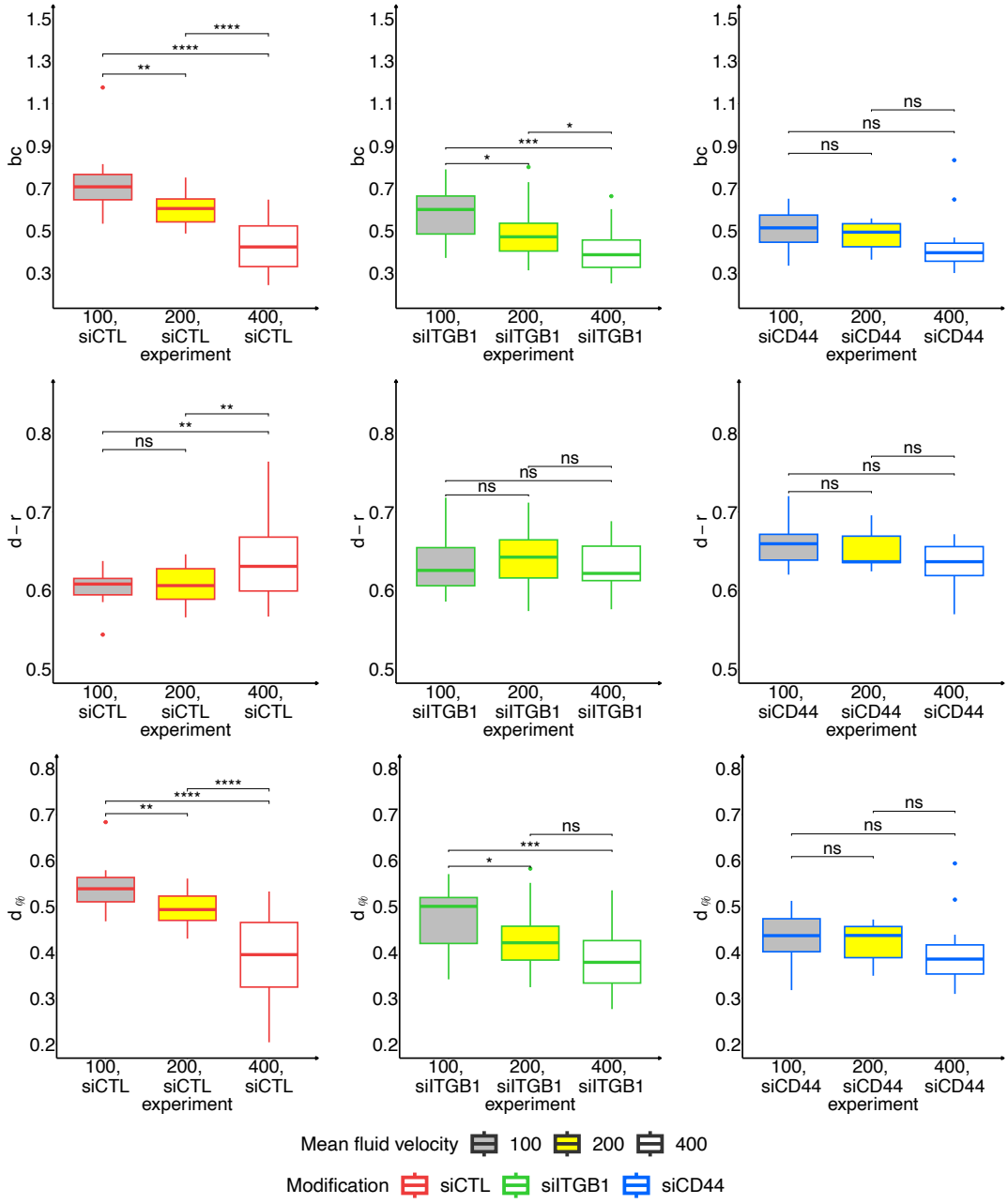

Figure 5: Box plots of the estimated parameters bc (top) and $d-r$ (middle) and the percentage of decrease in cell velocity $d_{\%}$ (bottom) for the 3 subcohorts (left: siCTL, middle: siTGB1, right: siCD44) and for the 3 cohorts of fluid velocities (x-axis: ~ 100 µm.s^{-1} for $G^{(1)}$, ~ 200 µm.s^{-1} for $G^{(3)}$, ~ 400 µm.s^{-1} for $G^{(3)}$). We substitute p-values with symbols such that: ns correspond to p$>10\%$, * to p$\leq 10\%$, ** to p$\leq 5\%$, *** to p$\leq 0.5\%$, and **** to p$\leq 0.05\%$.

Experiment \ Regression	Intercept estimate	Slope estimate	Slope *p-value*
siCTL$^{(1)}$	0.49	-0.0059	$\mathbf{9.3 \times 10^{-6}}$
siITGB1$^{(1)}$	0.57	-0.0073	$\mathbf{3.3 \times 10^{-10}}$
siCD44$^{(1)}$	0.59	-0.0033	$\mathbf{1.9 \times 10^{-2}}$
siCTL$^{(2)}$	0.53	-0.0085	$\mathbf{1.0 \times 10^{-2}}$
siITGB1$^{(2)}$	0.62	-0.018	$\mathbf{4.2 \times 10^{-9}}$
siCD44$^{(2)}$	0.61	-0.0051	0.28
siCTL$^{(3)}$	0.63	0.0029	0.81
siITGB1$^{(3)}$	0.70	-0.039	$\mathbf{6.7 \times 10^{-4}}$
siCD44$^{(3)}$	0.70	-0.063	$\mathbf{9.2 \times 10^{-7}}$

Table 3: *Linear regressions of the velocity values for all cohorts and subcohorts. Column 2: Intercept estimates (cell velocity value in the regression when $t = 0$). Column 3: Slope estimates. Column 4: p-value of the slope estimates. Superscripts refer to the experiment number with the fluid pressure values as in Subsection 2.2. The bold values are the p-values inferior to 2×10^{-2}.*

4.2 Parameters estimation

In what follows, when the parameters depend only on the velocity cohort, the 3 estimated values are given in a vector where the $\mathbf{c}^{th}$ value corresponds to the $\mathbf{c}^{th}$ cohort for $\mathbf{c} \in \{1, 2, 3\}$. We estimate the following values for the fluid parameters:

$$h_f^{m(1)} = 7.2 \times 10^{-6} \text{ m}, \quad \xi_f^{(\mathbf{c})} = (0.27,\, 0.13,\, 0.07), \quad \omega_f^{(\mathbf{c})} = (12.2,\, 24.4,\, 48.8) \text{ rad.s}^{-1},$$
$$\text{logit}(\varphi) \sim \mathcal{N}(\text{logit}(0.41), 1.63).$$

Using these estimated values, the mean velocity values are computed

$$\bar{u}_f^{(\mathbf{c})} = (99.8,\, 199.6,\, 399.3) \text{ µm.s}^{-1}.$$

Remark 4.1. *These estimated mean velocity values justify the normalization considered in Figure 3.*

For the adhesion parameters, Figure 4 shows the individual estimated values. It corresponds to the box plots of the estimated parameters bc (top) and $d - r$ (middle) and the resulting percentage of decrease in cell velocity $d_{\%}$ (bottom) for the 3 cohorts (left: pressure gradient fixed at $G^{(1)}$ middle: at $G^{(2)}$, right: at $G^{(3)}$) and for all considered cells (red: siCTL, green: siITGB1, blue: siCD44). We also add *p-values* ranges of the t-tests between the estimated values of parameters for different protein modifications at the same fluid pressure. To facilitate the comparison between the same protein modifications at different fluid pressure, Figure 5 shows the same estimated values but sorted by protein modifications instead of fluid pressure gradient. The *p-values* ranges of the t-tests between the estimated values of parameters at different fluid pressure gradients for the same proteins are shown.

Table 4 summarises the mean and standard deviations by cohorts and subcohorts. To facilitate the reading of this table, the mean values and the associated standard deviations are plotted in Figure 6.

To conclude this section, Figure 7 shows numerical fits compared to the experimental data. Independently of the fluid cohort, two typical behaviours are observed: the CTCs velocity either remains stationary or decreases. Therefore, we show examples of these behaviours for each velocity cohort in the siCTL case only. Velocity values are normalised by $2^{\mathbf{c}-1} \times 100$ µm.s^{-1} for each $\mathbf{c} \in \{1, 2, 3\}$.

Experiment \ Values	bc	$d-r$
siCTL$^{(1)}$	0.72 (0.15)	0.60 (0.02)
siITGB1$^{(1)}$	0.58 (0.11)	0.63 (0.04)
siCD44$^{(1)}$	0.51 (0.09)	0.66 (0.03)
siCTL$^{(2)}$	0.61 (0.08)	0.61 (0.02)
siITGB1$^{(2)}$	0.49 (0.13)	0.64 (0.03)
siCD44$^{(2)}$	0.47 (0.07)	0.65 (0.02)
siCTL$^{(3)}$	0.41 (0.12)	0.64 (0.05)
siITGB1$^{(3)}$	0.41 (0.11)	0.63 (0.03)
siCD44$^{(3)}$	0.43 (0.14)	0.63 (0.03)

Table 4: *Mean and standard deviation values of bc and $d-r$ for the all cohorts and subcohorts. The first value corresponds to the mean and the second value in parenthesis to the standard deviation. For both parameters the unit of measurement is s^{-1}.*

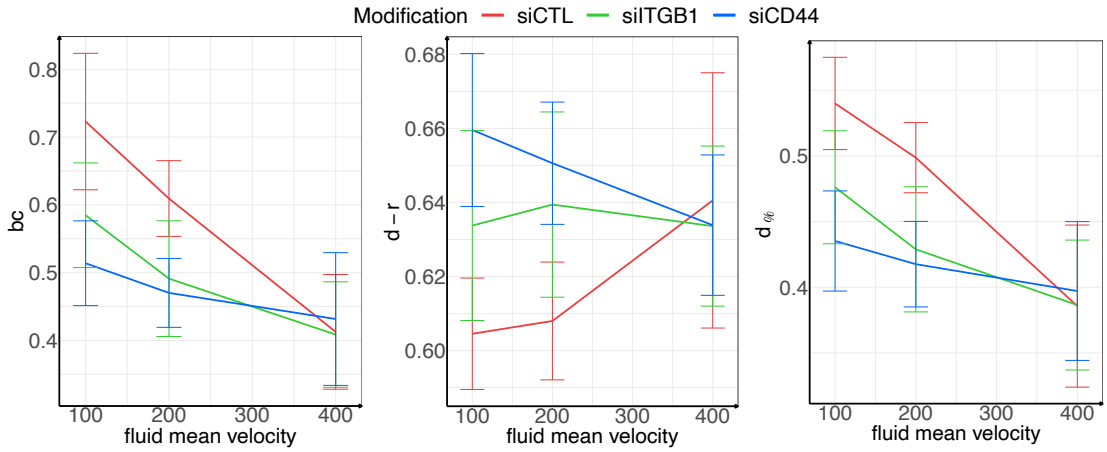

Figure 6: Representation of the mean values of bc (left), $d-r$ (middle) and $d_{\%}$ (right) for the different mean fluid velocities (x-axis) and for the different protein modifications (siCTL in red, siITGB1 in green and siCD44 in blue). The error bars correspond to the standard deviations.

5 Discussion

5.1 Data extraction and statistical analysis

One difficulty in detecting cells was to select the correct cells. Indeed, among the cells with an apparently free trajectory, we had to pick out the CTCs without collisions, without arrests, or without problems in tracking, e.g., due to proximity to other cells. This selection obviously has an impact on the results. This selection could be automated by a more efficient tracker, especially a fully automatic tracker even for large velocities. In addition, both the tracking method and the experimental setup only resulted in the measurement of translational cell velocities, which did not provide any information about possible rolling of the cells.

Concerning the statistical analysis of velocity data, significant differences between mean ve-

locities in almost all of the cohorts and subcohorts (*p-values* smaller than 2×10^{-3}, see Table 2) illustrate the importance of the fluid velocity and of the CD44 and ITGB1 proteins in the adhesion phenomenon. The mean velocities were not significantly different between siITGB1$^{(2)}$ and siCD44$^{(2)}$ ($p = 0.15$) and between siITGB1$^{(3)}$ and siCD44$^{(3)}$ ($p = 0.1$), probably due to the higher fluid velocity impeding adhesion. This is also supported by the linear regressions on the velocities, see Table 3). In each cohort and subcohort, the intercept smaller than 1 indicates the presence of adhesion, higher for lower fluid velocities and for siCTL cases. The slopes show a decelerating dynamics for 7 out of 9 subcohorts (*p-values* less than 2×10^{-2}). These values are negative but close to zero, indicating the presence of stationary velocity profiles, see Figure 7. The goal of the mathematical model – presented in Subsections 3.2 and 3.3 – was to understand and quantify these initial observations.

5.2 Fluid modeling

As for the fluid modeling, the choice of the pressure gradient under the cosinusoidal form has an important impact, since it can be shown that in our context the imaginary part i_f is larger than the real part r_f, which means that most of the oscillations of the cell velocities are under the cosinusoidal form. To make more complex assumptions, a better knowledge of the pump is needed.

As for the estimation of fluid parameters, the strong correlation between fluid and adhesion parameters leads to identification problems. For example, we observed that multiple values of the parameter pair $(bc, \bar{u}_f(h_f^m))$ resulted in similar fits. We then decided to constrain the fluid parameters using priors from the literature to allow more variation in the adhesion parameters. The prior value of h_f^m (only parameter appearing in the mean velocity values $\bar{u}_f$) has a strong impact on the results. The value has been selected to be coherent with the velocity measures with single-particles performed in [13] (see Figure 6-C). Its estimation led to mean velocity values very close to the estimated ones in [41], which are 100, 200 and 400 µm.s^{-1}. The prior of the angular velocity ω_f and its dependence on the pressure gradient can be derived directly from Figure 3-Top-Left (10 oscillations 5 s gives $\sim 10/5 \times 2\pi \sim$12.6 s^{-1}). As for the correction amplitude ξ_f, which appears in the amplitudes r_f and i_f in Equation (2), we have halved its value in each successive cohort. This is confirmed by the amplitudes observed in Figures 3 and 7. This last hypothesis was also confirmed by looking at the AIC for the case where ξ_f was constant (AIC=130019.6) as opposed to ξ_f depending on fluid pressure (AIC=129908.7). Of course, more complex hypotheses could be tested, but this would also require a better understanding of how the pump works.

5.3 Adhesion modeling

Modeling The adhesion dynamics is described by an ODE on the adhesion density. The modeling choice is built on Assumptions (3.1)-(3.2). Assumption (3.1) states constant binding rates in each velocity cohort. By doing so, the effects of velocity oscillations on the adhesion dynamics are neglected. Several biophysical studies investigated the relation between the load applied on a cell and its binding dynamics, and introduced catch bonds or slip bonds (see e.g [25–27]). These studies focus mainly on L-selectin bonds for leukocyte dynamics. For CTCs, it is known that CD44 mediating transient adhesion might bind glycocalyx, glycoproteins such as E-selectin or endothelial CD44, or fibronectin at the surface of endothelial cells. Stable adhesions are mediated by alpha5beta1 integrins that also bind fibronectin [14]. However, fluid velocities being quite high, capturing the binding response to variations of u_f seemed out-of-reach. Furthermore, the identification issues we had to deal with convinced us that the data were not well-suited

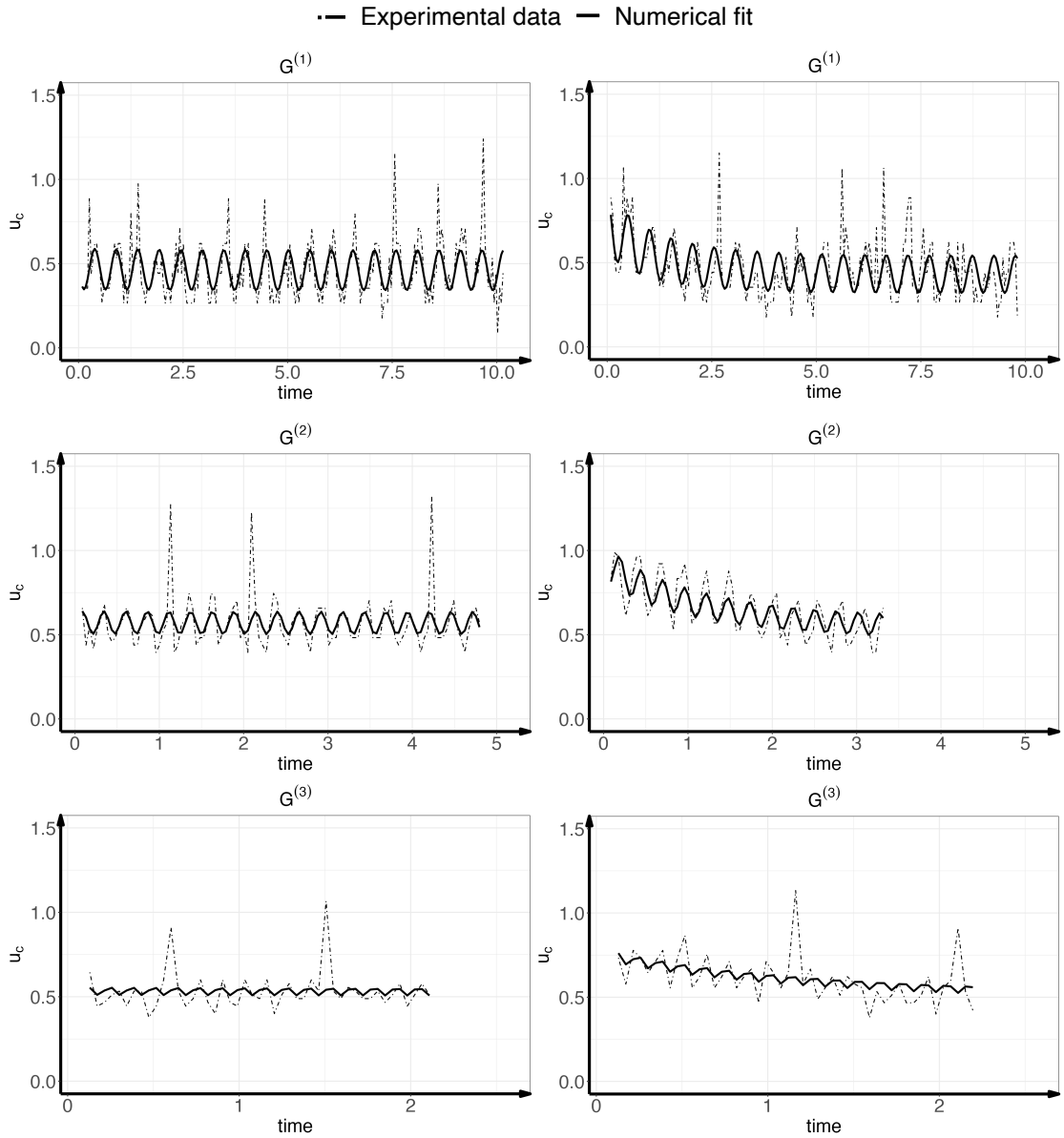

Figure 7: Numerical fits. The dot-dash line represents the experimental cells velocity and in solid, the fit that we obtain with Equation (6). Top: Pressure gradient fixed at $G^{(1)}$ corresponding to ~ 100 µm.s^{-1}, middle: $G^{(2)}$ corresponding to ~ 200 µm.s^{-1}, bottom: $G^{(3)}$ corresponding to ~ 400 µm.s^{-1}. Left: CTCs with a stationary regime, right: CTCs with a decreasing velocity. The time interval decreases since CTCs observation duration reduces with higher velocity.

for investigating this question. Assumption (3.1) then enables to derive an explicit solution for the bonds density over time given in Equation (4). It can be noted that this equation makes biological sense only when $d-r>0$, which is indeed found during the estimation of parameters. In this case, the bonds density increases exponentially and then saturates at $c/(d-r)$. When $d-r>0$, the asymptotic cell regime $d_{\%}$ cannot reach 1, preventing cell arrest. This shows that our modeling is not suitable to account for arrested cells.

In our model, cell velocity is given by the difference between the fluid velocity and an adhesion term. This formulation is classically found in other modeling approaches, see e.g [29, 31, 36, 37]. In a macroscopic setting, the adhesion term is proportional to the closed bonds density, and involves both geometric features and forces and torques exerted by the bonds. Rather than making this term explicit, we kept a minimal framework and compared three expressions.

The constant force model, given by $u_c(t) = u_f(t) - bN(t)$, accounts for constant binding forces at the cell scale, see [37]. The fluid-dependent force model writes $u_c(t) = u_f(t)(1-bN(t))$ and can be seen as a simplification of a model for elastic bonds given in [36]. Finally, the cell-dependent force model writes $u_c(t) = u_f(t) - bu_c(t)N(t)$, leading to Equation (5). This framework can be seen as a macroscopic viewpoint for the average force exerted by an elastic bond over its lifetime. Several studies show matching microscopic viewpoints involving structured bonds density capturing bonds elongation. In [29], the membrane at the cell rear moves away from the wall at a normal velocity proportional to u_c. In [34–36], elongation is the product of the bond's age and the cell velocity. Furthermore, in [34, 35], a scaling limit in fast bonds turnover and rigid forces allowed to justify rigorously a macroscopic adhesion term proportional to $u_c(t)$.

Assumption (3.2) consists in the choice of the cell-dependent force model over the others. The fluid-dependent force model (AIC=129910.6) slightly differs from the cell-dependent one (AIC=129908.7) in AIC. Using the constant force model strongly degrades the AIC (AIC=130066.8) showing that this assumption should be excluded.

Parameters estimation Concerning the adhesion parameters, we could only estimate bc, $d-r$ and τ. In contrast with the fluid whose behaviour is the same in all experiments, cell parameters vary from cell to cell. They were taken as the sum of a fixed population effect and of an individual random term. Several attempts have been realised to obtain the optimal parameters from which we could interpret the biological phenomenon at study. In particular, we have considered a covariate model for bc in order to integrate the cohorts effects. One could also add covariates with respect to subcohorts, but this seems only to complexify the definition of bc without improving the AIC. The same procedure can be applied to $d-r$. Again we have tried this strategy adding covariates respect to cohorts, subcohorts and adhesion group and both fixing $d-r$ in the population and considering individual variability. We got either similar or higher AICs (superior to 129920) in estimated parameters. Consequently, we considered only individual variability of $d-r$. These choices aim to reduce the number of estimated parameters, while making sure to have enough decelerating cells in each estimation group.

Interpretation of the estimated adhesion parameters Figures 4 and 5 show the estimated value of the parameter bc – accounting for elastic bonds and fluid friction forces and the binding rate – of the parameter $d-r$ – related to bonds instability, since $1/(d-r)$ is a typical adhesion lifetime at the macroscopic scale – and also the percentage of velocity decrease $d_{\%}$, given by a combination of the both of them. We have considered as significant *p-values* lower than 10% as it was a very natural threshold with only 6 values between 5% and 10% of which half of them below 6%. Figure 4 is sorted by fluid velocity. High fluid velocity is characterised by non-significant differences among protein modification experiments which means that adhesion is more difficult to establish. For low fluid velocity, both bc and $d_{\%}$ are decreasing with respect to

the protein modification, whereas $d - r$ is increasing. Consequently, we deduce that the control case is the one where adhesion is more efficient with larger binding dynamics and more stable bonds. On the other hand, depleting CD44 (siCD44) impedes the adhesion the most. Finally, the intermediate fluid velocity shows only significant differences between the control case and the modified conditions.

Figure 5 is sorted by protein modification. Both bc and $d_{\%}$ are decreasing with respect to the fluid velocity, whereas $d - r$ is increasing, but the results are not significant in the case siCD44 and for $d - r$ in the case siITGB1. With these exceptions, we deduce that fluid velocity has a significant impact on adhesion and the lower the velocity, the higher the possibility of observing this phenomenon. The fact that for $d - r$ we can not observe significant differences could also be related to the available data set and on the bias in the observation of cells deceleration.

5.4 Comparison with the literature

In the literature, the adhesive dynamics of MDA-MB-231 cells in a microfluidic device interacting with anti-EpCAM ligands-coated wall has been investigated in [40]. Sequential fitting of the computational model of [31] on mean translational velocities for several shear rates allowed to identify the average cell height, binding force, and bonds spring constant. Normalized cell velocities for all shear rates were successfully fitted by a generic exponentially decreasing curve, suggesting a strong dependence of the cell velocity magnitude on the fluid velocity, whereas it was not the case for the typical decay time. Several differences exist between our frameworks. From the biological viewpoint, the wall in [40] is passive, while ours is a monolayer of endothelial cells, whose flow-driven active behaviour in cell arrest has been observed [14]. Together with lower fluid velocities, it may explain their measures of smooth velocity decays until cell arrests, that were not observed in our case. Moreover, we worked with partial observations since cell velocities were not measured from their entrance in the experimental setting. On the other hand, we considered the time-oscillating fluid velocity that had to be reconstructed, and developed a mixed-effects calibration strategy able to deal with the individual cell velocities over time. In this setting, we obtained insights on the role of the fluid velocity that are consistent with previous observations [13, 14, 40]. Furthermore, our original and robust approach allowed to investigate the respective roles of ITGB1 and CD44 proteins in the cell dynamics, which affect both the magnitude of velocity decrease and the typical velocity decay time.

6 Conclusion and perspectives

In this work, we have attempted to characterise CTCs in the flow and their interaction with the vessel wall, relying on the *in vitro* experiments performed by Osmani and collaborators in [14, 41]. Whereas previous analyses focused on cell arrest, the use of the CSRT tracker allowed us to record trajectories and velocities of individual cells. We were able to analyse different cell cohorts with respect to three different values of fluid pressure gradient (below the threshold for efficient CTC adhesion found by Osmani and collaborators in [13]) and three different protein expressions (siCTL, the control case; siITGB1, depletion of ITGB1, integrin that promotes adhesion stabilisation; siCD44, depletion of CD44, protein involved in early adhesion). Statistical analysis of the mean of the extracted cell velocities and linear regression allowed the observation of a slowing behaviour over time, see Tables 2 and 3. This shows that adhesion is a continuous-time phenomenon involving CTCs in a fluid with a velocity below the threshold of 400 $\mu m.s^{-1}$.

Since the fluid velocity was not measured directly, we only knew the values of the pressure gradient generated by the peristaltic pump that made up the device. This lack of data was

compounded by our lack of knowledge about the pump. However, we were able to establish a Poiseuille regime and describe the fluid velocity as a combination of oscillatory functions induced by the pump and evident in the tracked cell velocity in Figure 3. We then focus on the modeling of the cell velocity. The oscillating Poiseuille flow was weakly coupled to a simple ODE model for cell adhesion that describes the cell velocity as the fluid velocity affected by bond formation and disruption.

Optimal parameters for our model were not easy to find. Indeed, there are practical problems with identifiability, mainly due to data noise and little information about the fluid parameters. Our strategy to overcome this problem is based on a mixed-effects model and careful selection of fluid parameter priors.

The well-designed parameter estimation has led to very attractive results, also from a biological point of view. Indeed, it turns out that a low fluid velocity favours a decrease of cell velocity and the formation of bonds. In contrast, a high fluid velocity makes it difficult to observe this adhesion phenomenon, even when both adhesion proteins are expressed. At the same time, we can demonstrate the role of CD44 and ITGB1 proteins in adhesion. Without the expression of CD44 (case siCD44), CTCs do not show a favourable deceleration behaviour, preventing the formation of the first (albeit weak) interactions with the wall. In the absence of ITGB1 expression (case siITGB1), the slowdown is less important than in the control case, but still present. Both pieces of information indicate that the ITGB1 protein, in contrast to the CD44 protein, does not promote early cell adhesion to the vessel wall, even if the combination of both leads to better adhesion.

These conclusions are reported in the *in vivo* experiments, whereas they could not be extracted from the *in vitro* experiments before our work. This highlights the quality of the strategy – based on mathematical modeling and data assimilation – we have developed. This work confirms that efficient CTC arrest relies on a 2-step mechanism: (1) an early step which requires a low energy but fast to engage CD44-dependent adhesion promotes the early arrest of CTCs in flow and (2) a high energy but slow to engage integrin beta1-dependent adhesion counteracts shear-ripping flow forces on arrested CTCs. This second step requires an early but transient arrest of the circulating cell.

As for the perspectives, the first one concerns the improvement of the CTC tracker from the experimental videos, since it is not fully automatic and has a great need of optimization. The second is the development of a mathematical model adapted to the *in vivo* experiments. These data should allow us to incorporate cell arrest into our model. The more complex geometry will require a more complex model of blood circulation. Finally, from a biological standpoint, it is possible to use the model presented to study and predict additional molecular modes involved in the arrest of CTCs at the vascular wall.

Author contributions AC and CE designed the study based on the biological data generated by NO in the team of JGG. GC and JG analyzed the data. AC and GC implemented the software code. AC, CE and GC interpreted the results. AC, CE and GC wrote the manuscript and JG the supplementary materials.

Acknowledgements

The work of JGG and NO has been funded by Plan Cancer 2014-2019 (OptoMetaTrap), CNRS IMAG'IN (to S.H. and J.G.G.) and by institutional funds from INSERM and the University of Strasbourg.

Declaration of interest

The authors declare no competing interests.

References

[1] H. Dillekås, M. S Rogers, and O. Straume. Are 90% of deaths from cancer caused by metastases? *Cancer Med.*, 8(12):5574–5576, 2019. URL https://doi.org/10.1002/cam4.2474.

[2] P. S. Steeg. Targeting metastasis. *Nat. Rev. Cancer*, 16(4):201–218, 2016. URL https://doi.org/10.1038/nrc.2016.25.

[3] D. Wirtz, K. Konstantopoulos, and P. C. Searson. The physics of cancer: the role of physical interactions and mechanical forces in metastasis. *Nat. Rev. Cancer*, 11(7):512–522, 2011. URL https://doi.org/10.1038/nrc3080.

[4] G. Follain, D. Herrmann, S. Harlepp, V. Hyenne, N. Osmani, S. C. Warren, P. Timpson, and J. G. Goetz. Fluids and their mechanics in tumour transit: shaping metastasis. *Nat. Rev. Cancer*, 20(2):107–124, 2020. URL https://doi.org/10.1038/s41568-019-0221-x.

[5] A. C. Obenauf and J. Massagué. Surviving at a distance: organ-specific metastasis. *Trends Cancer*, 1(1):76–91, 2015. URL https://doi.org/10.1016/j.trecan.2015.07.009.

[6] S. B. Lim, W. Di Lee, J. Vasudevan, W.-T. Lim, and C. T. Lim. Liquid biopsy: one cell at a time. *NPJ Precis. Oncol.*, 3(1):23, 2019. URL https://doi.org/10.1038/s41698-019-0095-0.

[7] M. Peralta, N. Osmani, and J. G. Goetz. Circulating tumor cells: Towards mechanical phenotyping of metastasis. *iScience*, 2022. URL https://doi.org/10.1016/j.isci.2022.103969.

[8] S. A. Joosse, T. M. Gorges, and K. Pantel. Biology, detection, and clinical implications of circulating tumor cells. *EMBO Mol. Med.*, 7(1):1–11, 2015. URL https://doi.org/10.15252/emmm.201303698.

[9] J. Liu, J. Lian, Y. Chen, X. Zhao, C. Du, Y. Xu, H. Hu, H. Rao, and X. Hong. Circulating tumor cells (ctcs): a unique model of cancer metastases and non-invasive biomarkers of therapeutic response. *Front. Genet.*, 12:734595, 2021. URL https://doi.org/10.3389/fgene.2021.734595.

[10] A. Ring, B. D. Nguyen-Straeuli, A. Wicki, and N. Aceto. Biology, vulnerabilities and clinical applications of circulating tumour cells. *Nat. Rev. Cancer*, 23(2):95–111, 2023. URL https://doi.org/10.1038/s41568-022-00536-4.

[11] Q.-Q. Huang, X.-X. Chen, W. Jiang, S.-L. Jin, X.-Y. Wang, W. Liu, S.-S. Guo, J.-C. Guo, and X.-Z. Zhao. Sensitive and specific detection of circulating tumor cells promotes precision medicine for cancer. *J. Cancer Metastasis Treat.*, 5:34, 2019. URL https://doi.org/10.20517/2394-4722.2018.94.

[12] K. A. Rejniak. Circulating Tumor Cells: When a Solid Tumor Meets a Fluid Microenvironment. In K. A. Rejniak, editor, *Systems Biology of Tumor Microenvironment*, volume 936, pages 93–106. Springer International Publishing, 2016. URL https://doi.org/10.1007/978-3-319-42023-3_5.

[13] G. Follain, N. Osmani, A. S. Azevedo, G. Allio, L. Mercier, M. A. Karreman, G. Solecki, M. J. García-León, O. Lefebvre, N. Fekonja, et al. Hemodynamic forces tune the arrest, adhesion, and extravasation of circulating tumor cells. *Dev. Cell*, 45(1):33–52, 2018. URL https://doi.org/10.1016/j.devcel.2018.02.015.

[14] N. Osmani, G. Follain, M. J. García-León, O. Lefebvre, I. Busnelli, A. Larnicol, S. Harlepp, and J. G. Goetz. Metastatic tumor cells exploit their adhesion repertoire to counteract shear forces during intravascular arrest. *Cell Rep.*, 28(10):2491–2500, 2019. URL https://doi.org/10.1016/j.celrep.2019.07.102.

[15] C. D. Paul, K. Bishop, A. Devine, E. L. Paine, J. R. Staunton, S. M. Thomas, J. R. Thomas, A. D. Doyle, L. M. Miller Jenkins, N. Y. Morgan, et al. Tissue architectural cues drive organ targeting of tumor cells in zebrafish. *Cell Syst.*, 9(2):187–206, 2019. URL https://doi.org/10.1016/j.cels.2019.07.005.

[16] I. Martínez-Pena, P. Hurtado, N. Carmona-Ule, C. Abuín, A. B. Dávila-Ibáñez, L. Sánchez, M. Abal, A. Chaachou, J. Hernández-Losa, S. R. Cajal, et al. Dissecting breast cancer circulating tumor cells competence via modelling metastasis in zebrafish. *Int. J. Mol. Sci.*, 22(17):9279, 2021. URL https://doi.org/10.3390/ijms22179279.

[17] G. I. Bell. Models for the specific adhesion of cells to cells. *Science*, 200(4342):618–627, 1978. URL https://doi.org/10.1126/science.347575.

[18] G. I. Bell, M. Dembo, and P. Bongrand. Cell adhesion. competition between nonspecific repulsion and specific bonding. *Biophys. J.*, 45(6):1051–1064, 1984. URL https://doi.org/10.1016/S0006-3495(84)84252-6.

[19] T. Erdmann and U. S. Schwarz. Stability of adhesion clusters under constant force. *Phys. Rev. Lett.*, 92(10):108102, 2004. URL https://doi.org/10.1103/PhysRevLett.92.108102.

[20] T. Erdmann and U. S. Schwarz. Adhesion clusters under shared linear loading: a stochastic analysis. *EPL*, 66(4):603, 2004. URL https://doi.org/10.1209/epl/i2003-10239-3.

[21] T. Erdmann and U. S. Schwarz. Impact of receptor-ligand distance on adhesion cluster stability. *Eur. Phys. J. E*, 22:123–137, 2007. URL https://doi.org/10.1140/epje/e2007-00019-8.

[22] D. A. Hammer and D. A. Lauffenburger. A dynamical model for receptor-mediated cell adhesion to surfaces. *Biophys. J.*, 52(3):475–487, 1987. URL https://doi.org/10.1016/S0006-3495(87)83236-8.

[23] M. Dembo, D. C. Torney, K. Saxman, and D. Hammer. The reaction-limited kinetics of membrane-to-surface adhesion and detachment. *Proc. Royal Soc. B*, 234(1274):55–83, 1988. URL https://doi.org/10.1098/rspb.1988.0038.

[24] D. A. Hammer and S. M. Apte. Simulation of cell rolling and adhesion on surfaces in shear flow: general results and analysis of selectin-mediated neutrophil adhesion. *Biophys. J.*, 63 (1):35–57, 1992. URL https://doi.org/10.1016/S0006-3495(92)81577-1.

[25] K.-C. Chang, D. Tees, and D. A. Hammer. The state diagram for cell adhesion under flow: leukocyte rolling and firm adhesion. *Proc. Natl. Acad. Sci.*, 97(21):11262–11267, 2000. URL https://doi.org/10.1073/pnas.200240897.

[26] K. E. Caputo, D. Lee, M. R. King, and D. A. Hammer. Adhesive dynamics simulations of the shear threshold effect for leukocytes. *Biophys. J.*, 92(3):787–797, 2007. URL https://doi.org/10.1529/biophysj.106.082321.

[27] M. T. Beste and D. A. Hammer. Selectin catch–slip kinetics encode shear threshold adhesive behavior of rolling leukocytes. *Proc. Natl. Acad. Sci.*, 105(52):20716–20721, 2008. URL https://doi.org/10.1073/pnas.0808213105.

[28] A. Efremov and J. Cao. Bistability of cell adhesion in shear flow. *Biophys. J.*, 101(5): 1032–1040, 2011. URL https://doi.org/10.1016/j.bpj.2011.07.026.

[29] L. Li, H. Tang, J. Wang, J. Lin, and H. Yao. Rolling adhesion of cell in shear flow: A theoretical model. *J. Mech. Phys. Solids*, 119:369–381, 2018. URL https://doi.org/10.1016/j.jmps.2018.07.013.

[30] L. Li, W. Kang, and J. Wang. Mechanical model for catch-bond-mediated cell adhesion in shear flow. *Int. J. Mol. Sci.*, 21(2):584, 2020. URL https://doi.org/10.3390/ijms21020584.

[31] C. B. Korn and U. S. Schwarz. Dynamic states of cells adhering in shear flow: from slipping to rolling. *Phys. Rev. E*, 77(4):041904, 2008. URL https://doi.org/10.1103/PhysRevE.77.041904.

[32] S. Reboux, G. Richardson, and O. E. Jensen. Bond tilting and sliding friction in a model of cell adhesion. *Proc. Royal Soc. A*, 464(2090):447–467, 2008. URL https://doi.org/10.1098/rspa.2007.0210.

[33] L. Preziosi and G. Vitale. A multiphase model of tumor and tissue growth including cell adhesion and plastic reorganization. *Math. Models Methods Appl. Sci.*, 21(09):1901–1932, 2011. URL https://doi.org/10.1142/S0218202511005593.

[34] V. Milišić and D. Oelz. On the asymptotic regime of a model for friction mediated by transient elastic linkages. *J. Math. Pures Appl.*, 96(5):484–501, 2011. URL https://doi.org/10.1016/j.matpur.2011.03.005.

[35] V. Milišić and D. Oelz. On a structured model for load-dependent reaction kinetics of transient elastic linkages mediating nonlinear friction. *SIAM Journal on Mathematical Analysis*, 47(3):2104–2121, 2015. ISSN 0036-1410, 1095-7154. doi: 10.1137/130947052. URL http://epubs.siam.org/doi/10.1137/130947052.

[36] B. Grec, B. Maury, N. Meunier, and L. Navoret. A 1d model of leukocyte adhesion coupling bond dynamics with blood velocity. *J. Theor. Biol.*, 452:35–46, 2018. URL https://doi.org/10.1016/j.jtbi.2018.02.021.

[37] C. Etchegaray and N. Meunier. A stochastic model for cell adhesion to the vascular wall. *J. Math. Biol.*, 79:1665–1697, 2019. URL https://doi.org/10.1007/s00285-019-01407-7.

[38] L. S. L. Cheung, X. Zheng, A. Stopa, J. C. Baygents, R. Guzman, J. A. Schroeder, R. L. Heimark, and Y. Zohar. Detachment of captured cancer cells under flow acceleration in a bio-functionalized microchannel. *Lab Chip*, 9(12):1721–1731, 2009. URL https://doi.org/10.1039/B822172C.

[39] L. S. L. Cheung, X. Zheng, L. Wang, R. Guzman, J. A. Schroeder, R. L. Heimark, J. C.

Baygents, and Y. Zohar. Kinematics of specifically captured circulating tumor cells in bio-functionalized microchannels. *J. Microelectromech. Syst.*, 19(4):752–763, 2010. URL https://doi.org/10.1109/JMEMS.2010.2052021.

[40] L. S. L. Cheung, X. Zheng, L. Wang, J. C. Baygents, R. Guzman, J. A. Schroeder, R. L. Heimark, and Y. Zohar. Adhesion dynamics of circulating tumor cells under shear flow in a bio-functionalized microchannel. *J. Microelectromech. Syst.*, 21(5):054033, 2011. URL https://doi.org/10.1088/0960-1317/21/5/054033.

[41] N. Osmani, G. Follain, V. Gensbittel, M. J. García-León, S. Harlepp, and J. G. Goetz. Probing intravascular adhesion and extravasation of tumor cells with microfluidics. *Metastasis: Methods and Protocols*, pages 111–132, 2021. URL https://doi.org/10.1007/978-1-0716-1350-4_8.

[42] A. Lukežič, T. Vojíř, L. Zajc, J. Matas, and M. Kristan. Discriminative correlation filter tracker with channel and spatial reliability. *Int. J. Comput. Vis.*, 126(7):671–688, 2018. URL https://doi.org/10.1007/s11263-017-1061-3.

[43] C. Poon. Measuring the density and viscosity of culture media for optimized computational fluid dynamics analysis of in vitro devices. *J. Mech. Behav. Biomed. Mater.*, 126:105024, 2022. URL https://doi.org/10.1016/j.jmbbm.2021.105024.

[44] T. W. Kao and C. Park. Experimental investigations of the stability of channel flows. part 1. flow of a single liquid in a rectangular channel. *J. Fluid Mech.*, 43(1):145–164, 1970. URL https://doi.org/10.1017/S0022112070002288.

[45] F. P. Incropera, D. P. DeWitt, T. L. Bergman, A. S. Lavine, et al. *Fundamentals of heat and mass transfer*, volume 6. Wiley New York, 1996.

[46] G. Ferreira, A. Sucena, L. L. Ferrás, F. T. Pinho, and A. M. Afonso. Hydrodynamic entrance length for laminar flow in microchannels with rectangular cross section. *Fluids*, 6(7):240, 2021. URL https://doi.org/10.3390/fluids6070240.

[47] J. R. Womersley. Method for the calculation of velocity, rate of flow and viscous drag in arteries when the pressure gradient is known. *Physiol. J.*, 127(3):553, 1955. URL https://doi.org/10.1113/jphysiol.1955.sp005276.

[48] H.-L. Ma and C.-H. Kuo. Theoretical analysis of an oscillatory plane poiseuille flow—a link to the design of vortex flow meter. *Phys. Fluids*, 29(5):053602, 2017. URL https://doi.org/10.1063/1.4984006.

[49] M. Lavielle. *Mixed effects models for the population approach: models, tasks, methods and tools*. CRC press, 2014.

[50] E. Kuhn and M. Lavielle. Maximum likelihood estimation in nonlinear mixed effects models. *Comput. Stat. Data Anal.*, 49(4):1020–1038, 2005. URL https://doi.org/10.1016/j.csda.2004.07.002.

[51] Monolix 2021R2, Lixoft SAS, a Simulations Plus company. URL https://monolix.lixoft.com.

[52] F. Hecht. New development in freefem++. *J. Numer. Math.*, 20(3-4):251–266, 2012. URL https://doi.org/10.1515/jnum-2012-0013.